Chemosphere 301 (2022) 134610

Contents lists available at ScienceDirect

Chemosphere

journal homepage: www.elsevier.com/locate/chemosphere

Highly selective cesium removal under acidic and alkaline conditions using a novel potassium aluminum thiostannate

Chenyang Yang [a], Yong Jae Suh [b,c,*], Kuk Cho [a,**]

[a] Department of Environmental Engineering, Pusan National University, 2 Busandaehak-ro 63beon-gil, Geumjeong-gu, Busan, 46241, Republic of Korea
[b] Resources Utilization Division, Korea Institute of Geoscience and Mineral Resources, 124 Gwahak-ro, Yuseong-gu, Daejeon, 34132, Republic of Korea
[c] Department of Resources Engineering, Korea University of Science and Technology, 217 Gajeong-ro, Yuseong-gu, Daejeon, 34113, Republic of Korea

HIGHLIGHTS

- A novel KAlSnS-3 adsorbent was designed and applied for cesium removal.
- Al^{3+} release contributed to the good adsorption performance of Cs^{+} at pH 2 and 12.
- The stable SnS_2-type crystal showed efficient adsorption of Cs^{+} in a wide pH range.
- The rapid kinetics led to 97.6% removal of Cs^{+} in the first minute.
- KAlSnS-3 maintained high selectivity toward Cs^{+} even under high salinity conditions.

GRAPHICAL ABSTRACT

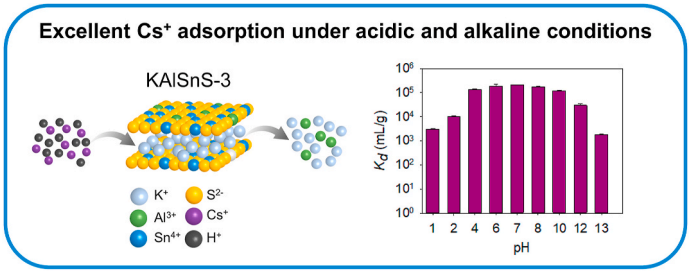

ARTICLE INFO

Handling Editor: Yongmei Li

Keywords:
Cesium
Sorption
Tin sulfide
Ion exchange
Chemical affinity

ABSTRACT

The pH values of nuclear wastewater are extremely low or high, which make the efficient removal of ^{137}Cs a major concern among the issues for safety management and environmental remediation. Existing metal sulfides for Cs^{+} adsorption have shown poor performance at acidic and alkaline conditions, and the reason has not been revealed yet. Herein, a novel potassium aluminum thiostannate (KAlSnS-3) adsorbent was designed and its Cs^{+} adsorption mechanism over a wide pH range was investigated. We hypothesized that Al^{3+} dopant on Sn^{4+} sites would allow stable adsorption for Cs^{+} upon its partial release at acidic and alkaline conditions. As a result, KAlSnS-3 demonstrated excellent adsorption performance across a broad pH range (1–13), and high selectivity toward Cs^{+}, even under high salinity conditions (in tap water $K_d = 3.12 \times 10^4$ mL/g; and in artificial seawater $K_d = 3.42 \times 10^3$ mL/g). KAlSnS-3 also exhibited rapid adsorption kinetics ($R = 97.6\%$ in the first minute), a remarkable adsorption capacity (259.31 mg/g), and a high distribution coefficient (2.09×10^5 mL/g) toward Cs^{+}. In addition, the high reusability of KAlSnS-3 was observed, suggesting its potential for real-world applications. The mechanism for enhancing performance at low and high pH values was discussed with the evidence of crystallinity, elemental concentrations, and binding energy of electrons based on the concept of electrostatic interactions and chemical affinity. In summary, this work provides insights into the mechanism of Cs^{+} removal under a wide pH range, and the

* Corresponding author. Resources Utilization Division, Korea Institute of Geoscience and Mineral Resources, 124 Gwahak-ro, Yuseong-gu, Daejeon, 34132, Republic of Korea.
** Corresponding author.
E-mail addresses: aumsuh@kigam.re.kr (Y.J. Suh), kukcho@pusan.ac.kr (K. Cho).

https://doi.org/10.1016/j.chemosphere.2022.134610
Received 30 January 2022; Received in revised form 28 March 2022; Accepted 11 April 2022
Available online 15 April 2022

impressive Cs^+ adsorption performance indicates the application potential of KAlSnS-3 in wastewater treatment.

1. Introduction

Nuclear energy is making a major contribution to mitigating climate change. More than 10% of the world's electricity is supplied by nuclear power plants (Zhiznin et al., 2020). However, the environmental issues associated with the generation of nuclear power are of great concern because of the production of highly radioactive wastewater. ^{137}Cs is the predominant radionuclide in nuclear wastewater that emits gamma and high-energy beta particles. Its long half-life (~30 years) poses a long-term risk to the environment and human health because it migrates easily with water (Hasan et al., 2021). Upon entering the body, it is taken up by muscles and stored over time because of its similar properties to those of K^+. Therefore, the efficient removal of Cs^+ from water is an urgent issue for safe nuclear power generation.

Adsorption is considered to be a promising method because it can extract trace Cs from water with ease (Crini and Lichtfouse, 2019). However, the much higher concentration of coexisting ions (Na^+, K^+, Mg^{2+}, and Ca^{2+}) than that of Cs^+ in nuclear wastewater limits the efficient removal of Cs^+ (Lee et al., 2021). Over the past decades, metal sulfides have been demonstrated to be a highly selective class of adsorbents for the removal of soft Lewis metal ions from water because of the existence of the soft Lewis base S^{2-} in the framework (Yang and Cho, 2021). However, there remain certain concerns regarding the use of current metal sulfides. For example, the wastewater generated from nuclear power plants exists in a wide pH range (Valsala et al., 2011; Xiao et al., 2017), and existing metal sulfides such as K-MPS-1 (Rathore et al., 2017), KTS-3 (Sarma et al., 2016), and InSnOS (Wang et al., 2019b) show poor adsorption performance toward Cs^+ under both highly acidic and alkaline conditions. And the reason for those poor performance has not been elucidated yet. Accordingly, investigating new design of metal sulfide adsorbents for Cs^+ remediation and their adsorption mechanism at extreme pH values are still of great significance.

Herein, we aimed to develop a novel metal sulfide and perform in-depth study of the mechanism under acidic, neutral, and alkaline conditions. For these objectives, a potassium aluminum thiostannate (KAlSnS-3) adsorbent was designed with the hypothesis that the release of structural Al^{3+} would result in a beneficial effect on the adsorption of Cs^+ from water. Aluminum sulfide is only stable at near neutral pH (Prokkola et al., 2020), and thus Al^{3+} will be released into water under acidic and alkaline conditions, providing additional adsorption driving force for Cs^+. In addition, Al^{3+} doping on Sn^{4+} may lead to enhanced K^+ intercalation because of the change of charge balance (Zhao et al., 2017). Our results demonstrated that KAlSnS-3 is a promising adsorbent with excellent adsorption characteristics, rapid kinetics, and high selectivity toward Cs^+. It is worth noting that a broad active pH range (1–13) was also achieved because of the preservation of robust SnS_2-type structure. The investigation of the Cs adsorption mechanism suggests that the ion exchange might be plausible by electrostatic interactions and chemical affinity as driving forces.

2. Materials and methods

2.1. Hydrothermal synthesis of KAlSnS-3

In brief, K_2CO_3 (24 mmol), tin powder (24 mmol), $Al(NO_3)_3{\cdot}9H_2O$ (3 mmol), and sulfur powder (120 mmol) were gently ground in an agate mortar until mixed. The mixture was then transferred to a polytetrafluoroethylene-lined autoclave, and ~1.5 mL of deionized water was added in drops. The autoclave was then placed in a furnace maintained at 200 °C for 24 h. After cooling to 25 °C, the synthesized KAlSnS-3 was separated by centrifugation at 10,000 rpm (RCF 11077×*g*), washed with deionized water and acetone for several cycles, and dried under vacuum at 60 °C overnight.

2.2. Adsorption experiments

All experiments in this study were conducted in at least three batches. A typical Cs^+ adsorption experiment was performed with a solid-to-liquid ratio of 1 g/L in a 30 mL vial. KAlSnS-3 (25 mg) was dispersed in a Cs^+ solution (25 mL) with a predetermined concentration and kept in an orbital shaker at 25 °C. Then, a 0.20 μm membrane filter (DISMIC cellulose acetate 25CS type, ADVANTEC, Japan) was used to separate the adsorbent. The concentration of Cs ions in the filtrate was determined using an atomic absorption spectrometer (AAnalyst 200, PerkinElmer, USA).

The adsorption kinetics were investigated by controlling the contact time (1–1080 min). Cs^+ adsorption experiments at different initial concentrations (4.94–1016 mg/L) were also conducted at 25 °C with a contact time of 3 h. Moreover, Cs^+ adsorption experiments were performed at various pH values. The Cs^+ solutions (~20 mg/L) with predetermined pH values of 1, 2, 4, 6, 7, 8, 10, 12, and 13 were prepared by adding HCl and NaOH solutions. The pH values were measured using an Orion Star A211 pH meter.

To evaluate the selectivity of KAlSnS-3 toward Cs^+, artificial seawater (ASW, Coralife) spiked with ~17.6 mg/L Cs^+ and local tap water (Busan, Korea) spiked with ~19.8 mg/L Cs^+ were used. Furthermore, the effect of coexisting common cations on the adsorption of Cs^+ was investigated at various salt concentrations (0.1–100 mM) by dissolving varying concentrations of NaCl, $MgCl_2{\cdot}6H_2O$, KCl, and $CaCl_2{\cdot}2H_2O$ in Cs^+ solutions. All adsorption experiments were performed at 25 °C, with a contact time of 3 h.

Finally, the reusability of KAlSnS-3 at different pH values was investigated. Specifically, 100 mg KAlSnS-3 was dispersed in 100 mL of 500 mg/L Cs^+ solution at pH 2, 7, and 12, and kept for 3 h under magnetic stirring. Next, KAlSnS-3 loaded with Cs^+ was regenerated by eluting Cs^+ in a 1 M KCl solution and washed with deionized water several times. The regenerated KAlSnS-3 was then used in successive Cs^+ adsorption experiments.

The adsorption tests in the presence of Cs^+ at pH 2, 7, and 12 were named Cs-loaded KAlSnS-3-pH-2, Cs-loaded KAlSnS-3-pH-7, and Cs-loaded KAlSnS-3-pH-12, respectively; whereas the samples in the absence of Cs^+ were named without the prefix "Cs-loaded," i.e., KAlSnS-3-pH-2, KAlSnS-3-pH-7, and KAlSnS-3-pH-12, respectively. The same convention was used for other samples, if not stated otherwise.

2.3. Calculations

The equilibrium adsorption capacity q_e (mg/g), distribution coefficient K_d (mL/g), removal efficiency R (%), and separation factor (SF) were calculated using the following equations:

$$q_e = [(C_o - C_e) \times V] / m \quad (1)$$

$$K_d = [(C_o - C_e) \times V \times 1000] / (C_e \times m) \quad (2)$$

$$R = [(C_o - C_e) / C_o] \times 100 \quad (3)$$

$$SF = \frac{K_d^M}{K_d^{Cs}} \quad (4)$$

where C_0 (mg/L) and C_e (mg/L) are the initial and final concentrations of Cs^+, respectively. V (L) is the volume of the Cs^+ solution, and m (g) is the mass of the adsorbent used in the experiments. K_d^M is the distribution

coefficient of competing ions (M represents Na^+, K^+, Mg^{2+}, and Ca^{2+}, respectively), and K_d^{Cs} is the distribution coefficient of Cs^+.

3. Results

3.1. General characterization of KAlSnS-3

Basic properties such as morphology, crystalline structure, and atomic composition were analyzed using various techniques. The sheet-like morphology of KAlSnS-3 was observed using field-emission scanning electron microscopy (FE-SEM) (Fig. 1a). The powder X-ray diffraction (PXRD) pattern of KAlSnS-3 (Fig. 1b) was similar to that of the KMS series adsorbents, which are based on robust SnS_2-type layers with M atoms (M = Mn, Mg, In) occupying the Sn sites and intercalated K^+ ions between layers (Manos and Kanatzidis, 2009; Mertz et al., 2013). The elemental mapping images of KAlSnS-3 (Fig. 1c) obtained by energy dispersive X-ray spectroscopy (EDS) indicated that K, Al, Sn, and S were homogeneously distributed in the sample.

The full survey spectrum (Fig. 1d) and the high-resolution spectra (Figure S1a–d) from X-ray photoelectron spectroscopy (XPS) showed the same composition of K, Al, Sn, and S. The peaks at 293.2 and 296.0 eV correspond to $2p_{3/2}$ and $2p_{1/2}$ of K^+ and the peak at 74.7 eV corresponds to Al 2p. The evident peaks of $3d_{5/2}$ and $3d_{3/2}$ of Sn^{4+} ions were centered at 486.4 and 494.8 eV, respectively. Moreover, the broad band ranges from 159 to 166 eV were deconvoluted into two peaks located at 161.3 and 162.5 eV, representing $2p_{3/2}$ and $2p_{1/2}$ of S^{2-} anions, respectively (Moulder et al., 1992).

The chemical formula of KAlSnS-3 was estimated to be $K_{1.61}Al_{0.30}Sn_3S_{6.74}$ (Table S1) and $K_{1.83}Al_{0.48}Sn_3S_{7.64}$ by EDS and inductively coupled plasma-optical emission spectrometry (ICP-OES), respectively, which confirmed the doping of lower charge valence Al^{3+} enhanced the amount of K^+ in KAlSnS-3 compared to that in KTS-3 ($K_{1.34}Sn_{3.26}S_{7.32}$) (Sarma et al., 2016). The N_2 adsorption–desorption isotherms and pore size distribution (Figure S2) revealed that KAlSnS-3 has a mesoporous microstructure with an average pore size of 30.96 nm, indicating an appropriate adsorbent structure (Wang et al., 2015).

3.2. Kinetics study

KAlSnS-3 exhibited excellent adsorption kinetics at different pHs. As shown in Fig. 2a, when the adsorbent was in contact with the Cs^+ solution for only 1 min at pH 7, the Cs^+ concentration decreased significantly from approximately 20 to 0.499 mg/L, with R = 97.6%. The equilibrium up to a removal efficiency of R = 98.6% was reached within 15 min. KAlSnS-3 showed fast kinetics even under extreme pH conditions. The removal efficiency of Cs^+ reached 89.4% within 10 min at pH 2 and 94.0% within 1 min at pH 12, which was similar to the removal efficiency under their equilibrium conditions (Figure S3). The adsorption experiments carried out at pH 2 and 12 resulted in the change of crystal structure, which will be discussed in detail in section 4.2. The high H^+ concentration at pH 2 led to a SnS_2-type crystal structure; whereas the high Na^+ concentration at pH 12 led to a $NaSnS_2$ structure. As these new crystal structures are highly stable under the extreme conditions, the Cs^+ adsorption kinetics moderately slowed down despite the high concentrations of competing species H^+ or Na^+.

The fast adsorption rate can be attributed to two factors. First, hierarchically structured nanosheets could be responsible for well-organized mass transfer channels, which can accelerate the diffusion of Cs^+ and K^+ into and out of the layer, respectively (Wang et al., 2020). The Cs^+ ions with a hydrated ionic radius of 2.19 Å (Marcus, 1994) should be similarly mobile in KAlSnS-3, Cs-loaded KAlSnS-3-pH-2, and Cs-loaded KAlSnS-3-pH-12, whose interlayer spacings were estimated to be 8.24 Å, 5.88 Å, and 8.46 Å from the PXRD patterns, respectively (Fig. S4). The kinetics of ion exchange for porous adsorbent materials is governed mostly by interparticle diffusion (Weber, 1984). In addition, soft Lewis base S^{2-} possesses a stronger affinity toward softer Lewis acid Cs^+ than that for harder Lewis acid K^+ (Pincus et al., 2020). Therefore, the adsorption mechanism might be the same for two extreme pH conditions as for the neutral condition. The fast adsorption kinetics of KAlSnS-3 is one of the key capabilities of efficient adsorbents.

3.3. Adsorption isotherms

Adsorption experiments for various initial concentrations of Cs^+

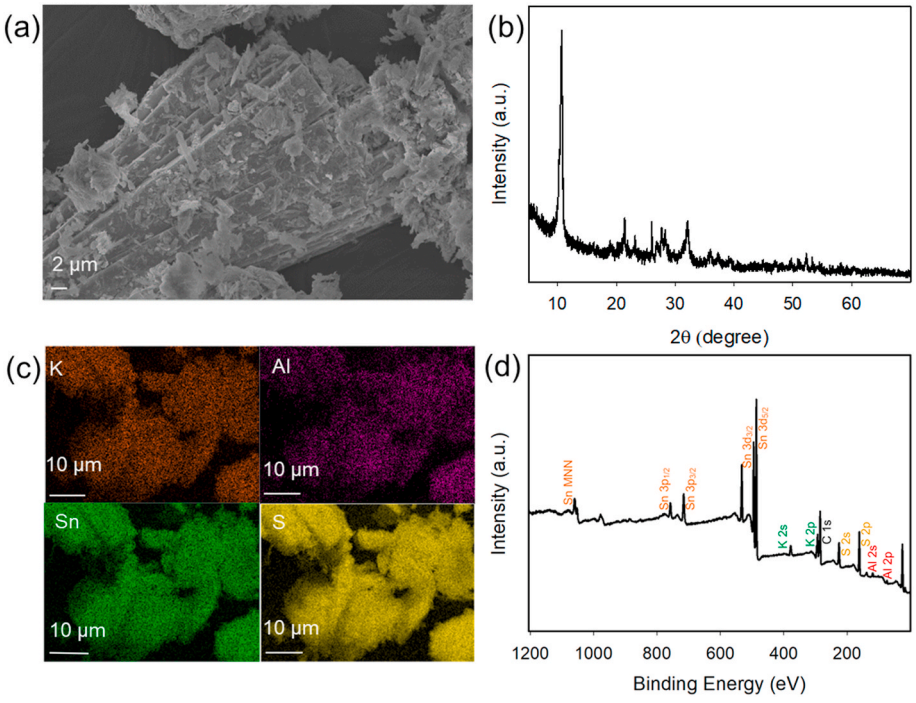

Fig. 1. Morphology and elemental composition of KAlSnS-3: (a) FE-SEM image; (b) PXRD pattern; (c) EDS elemental mapping images; and (d) XPS full survey spectrum.

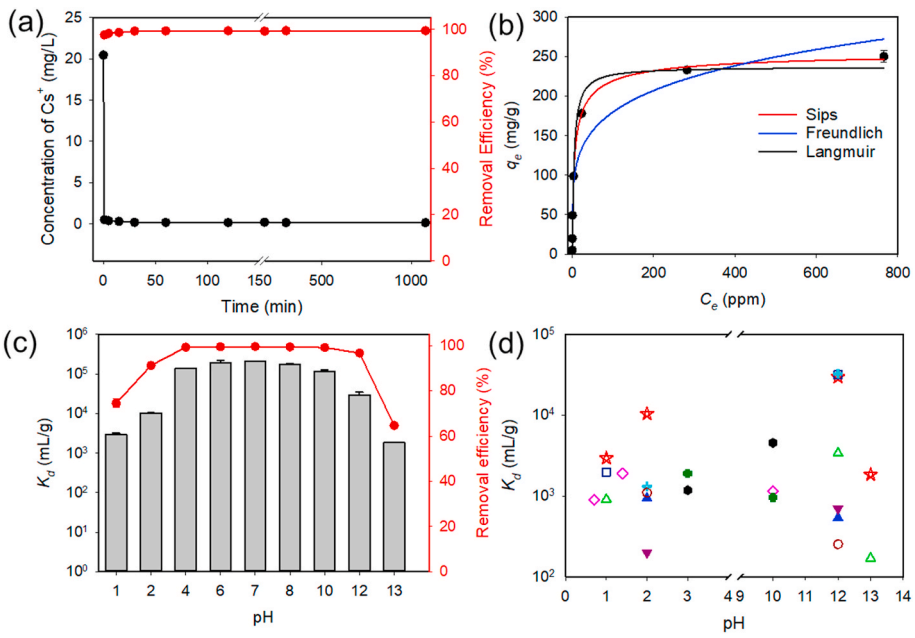

Fig. 2. Cs^+ adsorption performance of KAlSnS-3: (a) kinetics curve and removal efficiency (%) (C_0: ~20 mg/L, pH = 7); (b) equilibrium data, the solid curves represent the fitting by different isotherm models (C_0: 4.94–1016 mg/L, pH = 7); (c) distribution coefficient and removal efficiency at various pH levels (C_0: ~20 mg/L); and (d) comparison of distribution coefficients between various adsorbents at acidic and alkaline conditions: this study (☆), AgSnSe-1 (□), FJSM-SnS (◇), CuGeSe-1 (△), KATS-2 (+), InSnOS (▲), KTS-3 (○), KMS-2 (●), MIL-101-SO_3H (✚), and K-MPS-1 (▼).

were carried out to investigate the maximum adsorption capacity of KAlSnS-3. The equilibrium isotherm data were fitted using the Langmuir, Freundlich, and Sips adsorption isotherm models (see Section S3). The equilibrium adsorption capacity increased quickly with an increase in the equilibrium concentration at the beginning and then soon reached a plateau (Fig. 2b). This phenomenon can be explained by the fact that the initial Cs^+ concentration may have been the driving force for adsorption, and the slight increase in adsorption capacity at high initial concentrations indicates the saturation of the available binding sites of KAlSnS-3.

Table S2 shows the equilibrium constants obtained from isothermal modeling. The data show that the correlation coefficient for the Sips model was the highest (R^2 = 0.9995), indicating that it can fit the equilibrium data better than the Langmuir and Freundlich models. The maximum Cs^+ adsorption capacity calculated by the Sips model was 259.31 mg/g, which is comparable with that of KMS-1 (226 mg/g) (Manos and Kanatzidis, 2009), CuGeSe-1 (225.3 mg/g) (Liu et al., 2019), Na-GO (220 mg/g) (Lee et al., 2019), and Mont-EH-DT-KCuHCF (206.6 mg/g) (Zhang et al., 2017). This value is greater than that of $K_x[Bi_{4-x}Mn_xS_6]$ (164 mg/g) (Wang et al., 2019c), AgSnSe-1 (174.4 mg/g) (Ding et al., 2020), D-Clay/HCF Hydrogels (173 mg/g) (Zhang et al., 2020), Bn-CTS (57.1 mg/g) (Wang et al., 2019a), BFS-AMP (23.36 mg/g) (Xiao et al., 2019), and commercial AMP-PAN (81 mg/g) (Park et al., 2010). Although the adsorption capacity of KAlSnS-3 is lower than that of KTS-3 (280 mg/g) (Sarma et al., 2016), FJSM-SnS (408.91 mg/g) (Qi et al., 2015), PSi1/IPN-AOX (344.23 mg/g) (Dragan et al., 2020), InSnOS (537.7 mg/g) (Wang et al., 2019b), and K-MPS-1 (337.5 mg/g) (Rathore et al., 2017) (Table S3), its adsorption performance toward Cs^+ at acidic and alkaline conditions were better than that of most previously reported adsorbents because of its robust SnS_2-type structure, which will be discussed in section 4.

3.4. *pH-dependent Cs^+ adsorption*

As radioactive wastewater is usually very acidic or alkaline, it is of great significance to study the influence of pH on Cs^+ adsorption. KAlSnS-3 exhibited excellent Cs^+ adsorption performance across a broad pH range (Fig. 2c). Cs^+ is the only chemical species of cesium in aqueous media over a pH range of 0–14 as demonstrated in previous studies (Park et al., 2010; Yang and Cho, 2021). This confirms that the excellent Cs^+ adsorption performance of KAlSnS-3 in the pH range of 0–13 is not due to the precipitation of cesium into metal hydroxide. From pH 4 to 10, more than 99.2% of Cs^+ was removed and the K_d values ranged from 1.17×10^5 to 2.09×10^5 mL/g. This is owing to the excellent stability of KAlSnS-3 under these conditions, as its pristine crystal structure is retained (Figure S4a).

However, the K_d value decreased at pH 2 (1.04×10^4 mL/g) and pH 1 (2.94×10^3 mL/g). A similar trend was also observed in the high pH range ($K_d = 2.97 \times 10^4$ mL/g at pH 12; $K_d = 1.84 \times 10^3$ mL/g at pH 13). Although the K_d values decreased under both acidic and alkaline conditions, they were still comparable to those of AgSnSe-1 (Ding et al., 2020) and KATS-2 (Yang and Cho, 2021) and much higher than those of KTS-3 (Sarma et al., 2016), CuGeSe-1 (Liu et al., 2019), InSnOS (Wang et al., 2019b), K-MPS-1 (Rathore et al., 2017), MIL-101-SO_3H (Aguila et al., 2016), and KMS-2 (Mertz et al., 2013) (Fig. 2d). The reasons for KAlSnS-3 exhibiting excellent adsorption performance under acidic and alkaline conditions are presented in the discussion section.

3.5. *Effect of competing ions*

The complexity of the environment in a real water system motivated us to perform an applicability test on KAlSnS-3 in simulated and real water samples. In this study, local tap water (Busan, Korea) and ASW spiked with Cs were employed for adsorption experiments. The main components of tap water and ASW are listed in Table S4. As shown in Fig. 3a and Table S5, the K_d values of KAlSnS-3 to Cs^+ were 3.12×10^4 mL/g in tap water and 3.42×10^3 mL/g in ASW, which are higher than those of most adsorbents, including FJSM-SnS (Qi et al., 2015) and K-MPS-1 (Rathore et al., 2017). In contrast, the latter two adsorbents exhibited higher adsorption capacities than KAlSnS-3 (Table S3).

In order to determine the cation that interferes the most in the course of Cs^+ adsorption, the adsorption performance of KAlSnS-3 in solutions containing different salt species and concentrations (Na^+, Mg^{2+}, K^+, and Ca^{2+}) was investigated. As shown in Fig. 3b and S5, Cs^+ can be selectively adsorbed in the presence of competitive ions. The influence of divalent Mg^{2+} and Ca^{2+} on Cs^+ adsorption appeared to be stronger than that of monovalent Na^+ and K^+ at low concentrations (0.1–1 mM). The Debye lengths at 1 mM for monovalent and divalent cations were 9.61×10^{-9} and 4.81×10^{-9} m, respectively. It is presumed that long-range electrostatic interactions are still significant at these ranges

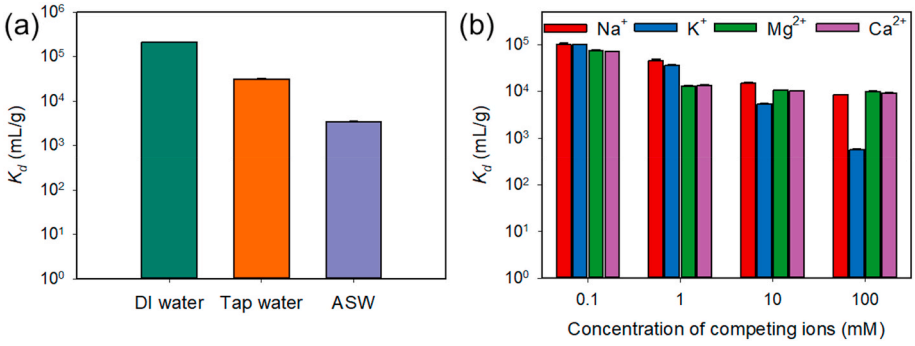

Fig. 3. (a) Selective adsorption of Cs^+ by KAlSnS-3 in different water systems; (b) variation in K_d of Cs^+ with increasing concentrations of Na^+, K^+, Mg^{2+}, and Ca^{2+} (C_0: ~20 mg/L).

(Israelachvili, 2011). Therefore, the negative surface of KAlSnS-3 has stronger electrostatic attraction to divalent ions than to monovalent ions.

As the electric double layer is compressed at a cation concentration of 10 mM or above, the influence of K^+ had the most significant effect on the adsorption of Cs^+. This can be explained in terms of chemical hardness or affinity. Soft Lewis base S^{2-} has a high affinity for Cs^+ and K^+ owing to its low chemical hardness (Table 1). This explains why KAlSnS-3 is selective toward Cs^+ and why K^+ as a competing species mostly affects the adsorption of Cs^+ when short-range surface forces govern their interaction.

4. Discussion

4.1. Driving forces for adsorption

The adsorption mechanism of KAlSnS-3 can be discussed in terms of electrostatic interactions and chemical hardness (Suh et al., 2015). Electrostatic interaction is a long-range force. As the metal sulfide layers possess negative charges, they exhibit a stronger electrical attraction to divalent cations than to monovalent cations. This occurs at a low ionic strength, particularly because the electrical double layer is rather thick (IhsanullahAbbas et al., 2016). In contrast, as the ionic strength increases, the electrical double layer is compressed to a narrow region, thereby increasing the importance of short-range interactions. Moreover, the much higher concentration of competing ions provides a higher probability of approaching the adsorbent surface and hence a higher opportunity to interact in close proximity to sulfur. According to kinetics theory, the collision frequency between two reactant species is proportional to the product of their concentrations. When the concentration of coexisting species, for example, K^+, increases from 1 to 100 mM, the chance to stay within the distance where a short-range interaction is dominant becomes 100-fold higher. Thus, chemical hardness plays a significant role in adsorption at high ionic strengths. The chemical hardness of a cation is determined by its ionization potential and electron affinity, partly representing the electron energy and configuration (Pearson, 1988). The two adsorption driving forces account for the selectivity trend among competing ions. Nevertheless, the soft base S^{2-} in KAlSnS-3 provides soft acids with an innate high affinity. Therefore, as a softer acid, Cs^+ can exchange interlayered harder K^+, even under high concentrations of competing ions such as Na^+, K^+, Mg^{2+}, and Ca^{2+}.

Table 1
Chemical hardness for competing cations.

Cation	Chemical hardness (eV) (Pearson, 1988; Lide, 2005)
Na^+	21.07
K^+	13.64
Cs^+	9.63
Mg^{2+}	32.55
Ca^{2+}	19.52

4.2. Mechanism of Cs^+ adsorption at different pH

The adsorption mechanisms at pH 7, pH 2, and pH 12, which are representative neutral, acidic, and alkaline conditions, are discussed. At a neutral pH of 7, the Cs^+ adsorption of KAlSnS-3 was examined using ICP-OES, SEM-EDS, PXRD, and XPS. First, the concentrations of K^+, Al^{3+}, Sn^{4+}, and Cs^+ in the feed solutions and filtrates were analyzed using ICP-MS and ICP-OES. The results showed that the molar ratio of the released K^+ to adsorbed Cs^+ was 0.971 (Table S6). Because the release of Al^{3+} under this condition is negligible, the main mechanism at pH 7 is likely to be ion exchange between K^+ and Cs^+. The elemental mapping for Cs-loaded KAlSnS-3 indicated that Cs^+ was homogeneously distributed on the surface (Figure S6b). Moreover, the EDS analysis in Table S1 shows that the amount of K^+ in Cs-loaded KAlSnS-3 decreased by 1.23 mol on the adsorption of 1.31 mol Cs^+, indicating ion exchange between K^+ and Cs^+.

In addition, the PXRD patterns show that the main peak of KAlSnS-3 shifted to a lower 2θ position after adsorption, and the d-spacing increased from 0.824 to 0.840 nm (Fig. 4a) (Sheth et al., 2022). This can be attributed to larger ionic radius of Cs^+ (1.67 Å) than that of K^+ (1.38 Å) (Shannon, 1976). The PXRD patterns also indicate that Cs-loaded KAlSnS-3-pH-7 was isostructural to KAlSnS-3 as the ion exchange was topotactic. Accordingly, the morphology of pristine KAlSnS-3 was preserved after adsorption (Figure S7c).

Another evidence of the ion exchange between K^+ and Cs^+ was revealed by the XPS spectra, showing that after Cs^+ adsorption, new Cs^+ characteristic peaks appeared, whereas the intensity of the K^+ characteristic peaks significantly decreased (Fig. 4b). This trend was clearer in the high-resolution spectra of Cs 3d and K 2p (Figure S8a and b). In addition, the high-resolution spectra of S 2p (Fig. 4c) after the adsorption at pH 7 show that the binding energy of S $2p_{3/2}$ and S $2p_{1/2}$ decreased from 161.28 to 161.25 eV and from 162.46 to 162.43 eV, respectively. The electron binding energy is negatively correlated with the electron density surrounding an atom (Whittles, 2018). Therefore, the decrease in binding energy could be ascribed to an increase in the electron density around S, resulting from the exchange of more electronegative K (Pauling scale of 0.82) for less electronegative Cs (0.79) (Yang et al., 2020).

Under the acidic condition at pH 2, the adsorption mechanism is largely affected by the behavior of H^+. As observed in the adsorption at pH 7, elemental mapping and SEM analysis showed that the elements were homogeneously distributed on the surface of Cs-loaded KAlSnS-3-pH-2, and the slab-like morphology of KAlSnS-3 was preserved after adsorption (Figs. S6a and S7b). However, the amount of Al in the adsorbent material greatly decreased from 0.30 to 0.07 mol (Table S1). The release of Al was also observed by ICP spectroscopy. Compared with

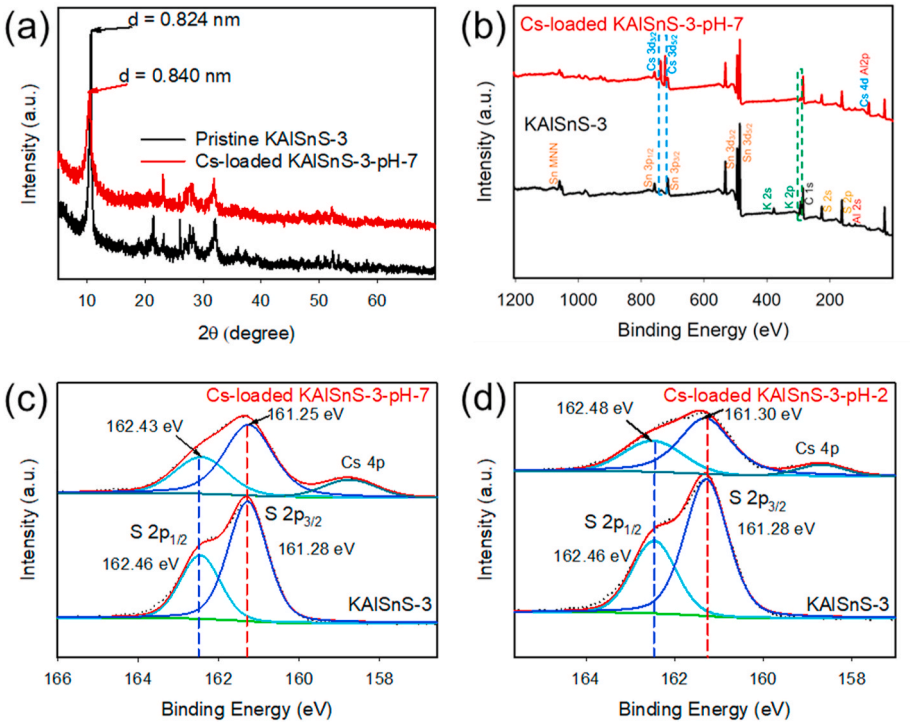

Fig. 4. (a) PXRD patterns and (b) full XPS survey spectra for KAlSnS-3 and Cs-loaded KAlSnS-3; and high-resolution XPS spectra of S 2p for (c) the pristine KAlSnS-3 and Cs-loaded KAlSnS-3-pH-7 and (d) the pristine KAlSnS-3 and Cs-loaded KAlSnS-3-pH-2.

the adsorption at pH 7, more K^+ was released after Cs^+ adsorption, such that the ratio of the total charge of the released K^+ and Al^{3+} to that of adsorbed Cs^+ was 3.210 (Table S6), which is far from unity. Upon the adsorption of Cs^+, the solution pH increased slightly from 2.07 to 2.20, indicating the simultaneous adsorption of H^+. Considering the amount of H^+, the ratio of the total charge of the released cations (K^+ and Al^{3+}) to that of adsorbed cations (Cs^+ and H^+) was estimated to be 1.096. This might indicate that the main adsorption mechanism under acidic conditions is the exchange of K^+ and Al^{3+} for Cs^+ and H^+. As Cs^+ competes with H^+ for the available active adsorption sites, the K_d value for Cs should decrease under acidic conditions. It should be noted that although protons are strong hard acids, they impede the adsorption of the soft acid Cs^+, resulting in a selectivity trend similar to that of K^+ as a competing species (see Figs. 2c and 3b).

The additional adsorption of H^+ at a low pH also affected the structure of the adsorbent. Contrary to the case of adsorption at pH 7, the binding energy of S 2p for the Cs-loaded KAlSnS-3-pH-2 increased (Fig. 4d). This is because more H^+ was adsorbed than Cs^+ (Table S6). The concentrations of Cs^+ and H^+ in the filtrate after adsorption decreased by 1.28 and 2.47 mM, respectively. Because protons have a much higher electronegativity (2.20) than Cs^+ (0.79) and K^+ (0.82), the adsorption of more H^+ caused the electron density around S to decrease.

To examine the effect of H^+ on the adsorbent structure more closely, separate adsorption experiments were performed using solutions of pH 1 and 2 in the absence of Cs^+. The PXRD pattern of the sample at pH 2 shows that the characteristic peak of the pristine KAlSnS-3 at 10.7° shifted to 12.2° and a new Bragg peak at 15.0° appeared at the same time (Figure S4b). With a further increase in H^+ concentration to 1 mol/L, the original characteristic peak disappeared and the peaks corresponding to an H-type product, which is isostructural to SnS_2, appeared instead (pattern for pH 1 in Figure S4b) (Manos et al., 2009; Wang et al., 2019c). This can be attributed to the exchange of larger K^+ ions for smaller H^+ ions. Furthermore, EDS analysis revealed the ion exchange between K^+ and H^+ when the amount of K^+ greatly decreased from 1.61 to 0.28 mol (KAlSnS-3-pH-2 in Table S1). Contrary to the case in the presence of Cs^+, a decrease in the amount of Al^{3+} was not observed. This contradictory behavior can be explained as follows. The electron density around S in Cs-loaded KAlSnS-3-pH-2 is higher than that in KAlSnS-3-pH-2 because the electronegativity of Cs^+ is lower than that of H^+. Hence, the polarity of the Al–S bond in Cs-loaded KAlSnS-3-pH-2 was higher than that in KAlSnS-3-pH-2 (Mortier et al., 1986; Sanderson, 2012). The polarity of the covalent bond is negatively related to its strength. Thus, a weaker Al–S bond in Cs-loaded KAlSnS-3-pH-2 might promote the release of Al^{3+} (Gibbs et al., 1998).

Finally, we examined the adsorption mechanisms under alkaline conditions at pH 12. The EDS analysis showed that the amount of Na^+ in Cs-loaded KAlSnS-3-pH-12 (0.09 mol) was much lower than that in KAlSnS-3-pH-12 (1.02 mol) upon the adsorption of Cs^+ (Table S1). This indicates that Cs^+ was preferentially adsorbed while competing with Na^+; thus, the distribution coefficient, K_d, for Cs^+ slightly decreased. Considering the adsorption of both Cs^+ and Na^+, the molar ratio of the released K^+ to the total adsorbates obtained from the ICP spectroscopy analysis was 0.907, indicating the exchange of K^+ for both Cs^+ and Na^+ (Table S6).

According to the elemental mapping analysis, the adsorption sample Cs-loaded KAlSnS-3-pH-12 showed a homogeneous elemental distribution over the adsorbent with a lower amount of K and Al (Figure S6c). Precise quantitative analysis by ICP spectroscopy revealed that in addition to K^+, a significant amount of Al^{3+} and Sn^{4+} were also released (Table S6). Incorporating the released sites of Al^{3+} and Sn^{4+} to the released K^+ sites, the ratio of the released sites to the adsorbed sites was 1.701, much higher than the 0.907 for the instance when only K^+ was counted (Table S6). Therefore, the available adsorption sites other than K^+ did not seem to be active in the adsorption of Cs^+ and Na^+. Indeed, the release of Al^{3+} and Sn^{4+} may lead to the transformation of KAlSnS-3. Al in Al_2S_3 reacts with NaOH to form $Na(Al(OH)_4)$ because of the low stability of Al_2S_3 at a high pH. The dissolution of Al_2S_3 may trigger the release of Sn^{4+} owing to the weakened crystal structure (Gensemer and Playle, 1999). Unlike Al^{3+}, Sn^{4+} forms a stable bond with S^{2-} at a high pH because of a higher bond dissociation energy (467 kJ/mol) than that of Al–S (332 kJ/mol) (Lide, 2005). Chalcogenides with high crystallinity can be synthesized under alkaline conditions (Xie et al., 2015). Thus, the

dissociation of Al–S resulted in the transformation of KAlSnS-3 into $NaSnS_2$ with high crystallinity while preserving the SnS_2-type crystal (Figure S4c), which is stable over a wide pH range (Manos and Kanatzidis, 2009). This is illustrated in the SEM image of Cs-loaded KAlSnS-3-pH-12, which exhibited a thicker slab-like morphology than that of the pristine KAlSnS-3 (Figure S7d). The preservation of the SnS_2-type crystal structure accounts for the good adsorption performance of KAlSnS-3 under alkaline conditions.

4.3. Effect of Al^{3+} release on the reusability of KAlSnS-3

To investigate the reusability of KAlSnS-3, adsorption experiments were repeated after performing a set of adsorption–desorption experiments for the same adsorbent. In previous studies (Goyal et al., 2020; Zhou et al., 2021), Cs^+ solutions with low initial concentrations were used for the reusability test, which made it difficult to determine the true extent of reusability because of the unoccupied adsorption sites remaining after the first adsorption experiment. Thus, we employed high concentration Cs^+ solutions (500 mg/L) to ensure the saturation of most available adsorption sites based on the equilibrium data (Fig. 2b).

The equilibrium adsorption capacities of pristine and regenerated KAlSnS-3 toward Cs^+ at various pH values are shown in Figure S9. The regenerated sample KAlSnS-3-pH-7 exhibited nearly the same equilibrium adsorption capacity as that of pristine KAlSnS-3 owing to its excellent stability. In addition, the regenerated adsorbents at pH 2 and 12 showed nearly the same capacity as that of the pristine KAlSnS-3 under the respective conditions. It should be noted that the roles of Al^{3+} in this study are to form an acidic- and alkaline-stable SnS_2-type structure and to supply negative electrical environment for cation exchange. During the adsorption experiment at pH 2, the release of the trivalent structural Al^{3+} makes the interlayer more negative, which is immediately balanced by the interlayered Cs^+ and H^+ ions. Then the regeneration process in 1 M KCl solution causes the Cs^+ and H^+ ions adsorbed in Cs-loaded KAlSnS-3-pH-2 to be exchanged with K^+ ions. Similarly, at pH 12, the interlayered Cs^+ and Na^+ in Cs-loaded KAlSnS-3-pH-12 are exchanged with K^+ during the regeneration. The regenerated adsorbent with some vacant sites for the structural Al^{3+} did not show deterioration of the adsorption capacity. As far as the robust SnS_2-type crystal structure of KAlSnS-3 is preserved at pH 2 and 12 as mentioned in section 4.2, regeneration might not decrease the adsorption ability of the adsorbent. The robust crystal structure of KAlSnS-3 suggests its high reusability at various pH values in real-world applications.

5. Conclusions

The radioactive ^{137}Cs contaminated water system is quite complex: not only is the salinity high, but the pH value is very acidic or alkaline, which prompts the discovery of a highly-selective adsorbent toward Cs^+ under harsh conditions. In this study, we developed a novel metal sulfide, KAlSnS-3, by doping low-valent Al^{3+} on Sn^{4+} sites of SnS_2. Under harsh acidic and alkaline conditions, the release of Al^{3+} due to low stability of Al_2S_3 did not induce the general tendency to decrease adsorption capability. On the contrary, the structural transformation in course of adsorption-desorption processes from KAlSnS-3 to Al-deficient $KSnS_2$ maintained its high Cs^+ adsorption capacity and high reusability. The contribution of releasable dopant to adsorption provides valuable insights into the design of metal sulfide adsorbents for Cs^+-contained wastewater remediation, and offers a significant environmental benefit for the real applications that would prohibit radioactive discharge into the environment.

Credit author statement

Chenyang Yang: Conceptualization, Methodology, Investigation, Writing - original draft. **Yong Jae Suh**: Writing - review & editing. **Kuk Cho**: Validation, Supervision, Writing - review & editing.

Funding sources

This work was supported by the Basic Science Research Program through the National research foundation (NRF) of Korea funded by the Ministry of Education, Republic of Korea [2020R1A6A1A03044834]; and the Basic Research Project [GP2020-013, 22–3212] of the Korea Institute of Geoscience and Mineral Resources (KIGAM) funded by the Ministry of Science and ICT of Korea.

Declaration of competing interest

The authors declare that they have no known competing financial interests or personal relationships that could have appeared to influence the work reported in this paper.

Appendix A. Supplementary data

Supplementary data to this article can be found online at https://doi.org/10.1016/j.chemosphere.2022.134610.

References

Aguila, B., Banerjee, D., Nie, Z., Shin, Y., Ma, S., Thallapally, P.K., 2016. Selective removal of cesium and strontium using porous frameworks from high level nuclear waste. Chem. Commun. 52, 5940–5942.
Crini, G., Lichtfouse, E., 2019. Advantages and disadvantages of techniques used for wastewater treatment. Environ. Chem. Lett. 17, 145–155.
Ding, D., Cheng, L., Wang, K.-Y., Liu, H.-W., Sun, M., Wang, C., 2020. Efficient Cs^+–Sr^{2+} separation over a microporous silver selenidostannate synthesized in deep eutectic solvent. Inorg. Chem. 59, 9638–9647.
Dragan, E.S., Humelnicu, D., Ignat, M., Varganici, C.D., 2020. Superadsorbents for strontium and cesium removal enriched in amidoxime by a homo-IPN strategy connected with porous silica texture. ACS Appl. Mater. Interfaces 12, 44622–44638.
Gensemer, R.W., Playle, R.C., 1999. The bioavailability and toxicity of aluminum in aquatic environments. Crit. Rev. Environ. Sci. Technol. 29, 315–450.
Gibbs, G., Hill, F., Boisen, M., Downs, R., 1998. Power law relationships between bond length, bond strength and electron density distributions. Phys. Chem. Miner. 25, 585–590.
Goyal, N., Gao, P., Wang, Z., Cheng, S., Ok, Y.S., Li, G., Liu, L., 2020. Nanostructured chitosan/molecular sieve-4A an emergent material for the synergistic adsorption of radioactive major pollutants cesium and strontium. J. Hazard Mater. 392, 122494.
Hasan, M.N., Shenashen, M.A., Hasan, M.M., Znad, H., Awual, M.R., 2021. Assessing of cesium removal from wastewater using functionalized wood cellulosic adsorbent. Chemosphere 270, 128668.
Ihsanullah, Abbas, A., Al-Amer, A.M., Laoui, T., Al-Marri, M.J., Nasser, M.S., Khraisheh, M., Atieh, M.A., 2016. Heavy metal removal from aqueous solution by advanced carbon nanotubes: critical review of adsorption applications. Separ. Purif. Technol. 157, 141–161.
Israelachvili, J.N., 2011. Intermolecular and Surface Forces, third ed. Academic Press, Amsterdam.
Lee, H., Lee, K., Kim, S.O., Lee, J.-S., Oh, Y., 2019. Effective and sustainable Cs^+ remediation via exchangeable sodium-ion sites in graphene oxide fibers. J. Mater. Chem. 7, 17754–17760.
Lee, Y., Park, C.W., Kim, H.J., Kim, S.-J., Lee, T.S., Yang, H.-M., 2021. Sulfur-encapsulated zeolite micromotors for the selective removal of cesium from high-salt water with accelerated cleanup times. Chemosphere 276, 130190.
Lide, D.R., 2005. CRC Handbook of Chemistry and Physics, Internet Version. CRC Press, Boca Raton, FL.
Liu, H.-W., Wang, K.-Y., Ding, D., Sun, M., Cheng, L., Wang, C., 2019. Deep eutectic solvothermal synthesis of an open framework copper selenidogermanate with pH-resistant Cs^+ ion exchange properties. Chem. Commun. 55, 13884–13887.
Manos, M.J., Kanatzidis, M.G., 2009. Highly efficient and rapid Cs^+ uptake by the layered metal sulfide $K_{2x}Mn_xSn_{3-x}S_6$ (KMS-1). J. Am. Chem. Soc. 131, 6599–6607.
Manos, M.J., Petkov, V.G., Kanatzidis, M.G., 2009. $H_{2x}Mn_xSn_{3-x}S_6$ (x = 0.11–0.25): a novel reusable sorbent for highly specific mercury capture under extreme pH conditions. Adv. Funct. Mater. 19, 1087–1092.
Marcus, Y., 1994. A simple empirical model describing the thermodynamics of hydration of ions of widely varying charges, sizes, and shapes. Biophys. Chem. 51, 111–127.
Mertz, J.L., Fard, Z.H., Malliakas, C.D., Manos, M.J., Kanatzidis, M.G., 2013. Selective removal of Cs^+, Sr^{2+}, and Ni^{2+} by $K_{2x}Mg_xSn_{3-x}S_6$ (x = 0.5–1) (KMS-2) relevant to nuclear waste remediation. Chem. Mater. 25, 2116–2127.
Mortier, W.J., Ghosh, S.K., Shankar, S., 1986. Electronegativity-equalization method for the calculation of atomic charges in molecules. J. Am. Chem. Soc. 108, 4315–4320.
Moulder, J.F., Stickle, W.F., Sobol, P.E., Bombem, K.D., 1992. Handbook of X-Ray Photoelectron Spectroscopy. Perkin-Elmer Corporation.
Park, Y., Lee, Y.-C., Shin, W.S., Choi, S.-J., 2010. Removal of cobalt, strontium and cesium from radioactive laundry wastewater by ammonium molybdophosphate–polyacrylonitrile (AMP–PAN). Chem. Eng. J. 162, 685–695.

Pearson, R.G., 1988. Absolute electronegativity and hardness: application to inorganic chemistry. Inorg. Chem. 27, 734–740.
Pincus, L.N., Rudel, H.E., Petrović, P.V., Gupta, S., Westerhoff, P., Muhich, C.L., Zimmerman, J.B., 2020. Exploring the mechanisms of selectivity for environmentally significant oxo-anion removal during water treatment: a review of common competing oxo-anions and tools for quantifying selective adsorption. Environ. Sci. Technol. 54, 9769–9790.
Prokkola, H., Nurmesniemi, E.-T., Lassi, U., 2020. Removal of metals by sulphide precipitation using Na_2S and HS^--Solution. ChemEngineering 4, 51.
Qi, X.-H., Du, K.-Z., Feng, M.-L., Li, J.-R., Du, C.-F., Zhang, B., Huang, X.-Y., 2015. A two-dimensionally microporous thiostannate with superior Cs^+ and Sr^{2+} ion-exchange property. J. Mater. Chem. 3, 5665–5673.
Rathore, E., Pal, P., Biswas, K., 2017. Reversible and efficient sequestration of cesium from water by the layered metal thiophosphate $K_{0.48}Mn_{0.76}PS_3 \cdot H_2O$. Chem. Euro. J. 23, 11085–11092.
Sanderson, R., 2012. Chemical Bonds and Bonds Energy. Elsevier, Amsterdam.
Sarma, D., Malliakas, C.D., Subrahmanyam, K.S., Islam, S.M., Kanatzidis, M.G., 2016. $K_{2x}Sn_{4-x}S_{8-x}$ (x = 0.65–1): a new metal sulfide for rapid and selective removal of Cs^+, Sr^{2+} and UO_2^{2+} ions. Chem. Sci. 7, 1121–1132.
Shannon, R., 1976. Revised effective ionic radii and systematic studies of interatomic distances in halides and chalcogenides. Acta Crystallogr. A 32, 751–767.
Sheth, Y., Dharaskar, S., Chaudhary, V., Khalid, M., Walvekar, R., 2022. Prospects of titanium carbide-based MXene in heavy metal ion and radionuclide adsorption for wastewater remediation: a review. Chemosphere 293, 133563.
Suh, Y.J., Chae, J.W., Jang, H.D., Cho, K., 2015. Role of chemical hardness in the adsorption of hexavalent chromium species onto metal oxide nanoparticles. Chem. Eng. J. 273, 401–405.
Valsala, T., Sonavane, M., Kore, S., Sonar, N., De, V., Raghavendra, Y., Chattopadyaya, S., Dani, U., Kulkarni, Y., Changrani, R., 2011. Treatment of low level radioactive liquid waste containing appreciable concentration of TBP degraded products. J. Hazard Mater. 196, 22–28.
Wang, K., Ma, H., Pu, S., Yan, C., Wang, M., Yu, J., Wang, X., Chu, W., Zinchenko, A., 2019a. Hybrid porous magnetic bentonite-chitosan beads for selective removal of radioactive cesium in water. J. Hazard Mater. 362, 160–169.
Wang, L., Pei, H., Sarma, D., Zhang, X.-M., MacRenaris, K., Malliakas, C.D., Kanatzidis, M.G., 2019b. Highly selective radioactive $^{137}Cs+$ capture in an open-framework oxysulfide based on supertetrahedral cluster. Chem. Mater. 31, 1628–1634.
Wang, L., Shi, C., Pan, L., Zhang, X., Zou, J.-J., 2020. Rational design, synthesis, adsorption principles and applications of metal oxide adsorbents: a review. Nanoscale 12, 4790–4815.
Wang, R., Chen, H., Xiao, Y., Hadar, I., Bu, K., Zhang, X., Pan, J., Gu, Y., Guo, Z., Huang, F., 2019c. $K_x[Bi_{4-x}Mn_xS_6]$, design of a highly selective ion exchange material and direct gap 2D semiconductor. J. Am. Chem. Soc. 141, 16903–16914.
Wang, X., Lu, M., Wang, H., Pei, Y., Rao, H., Du, X., 2015. Three-dimensional graphene aerogels–mesoporous silica frameworks for superior adsorption capability of phenols. Separ. Purif. Technol. 153, 7–13.
Weber, W.J., 1984. Evolution of a technology. J. Environ. Eng. 110, 899–917.
Whittles, T.J., 2018. Electronic Characterisation of Earth-Abundant Sulphides for Solar Photovoltaics. Springer.
Xiao, C., Hassanzadeh Fard, Z., Sarma, D., Song, T.-B., Xu, C., Kanatzidis, M.G., 2017. Highly efficient separation of trivalent minor actinides by a layered metal sulfide ($KInSn_2S_6$) from acidic radioactive waste. J. Am. Chem. Soc. 139, 16494–16497.
Xiao, F., Huang, T., Zhang, S., Liu, L., Wang, C., Peng, G., He, S., 2019. Optimization analysis and mechanism exploration on the removal of cesium and the solidification of secondary residue wastes in electrokinetics. J. Clean. Prod. 233, 1207–1220.
Xie, B.-B., Hu, B.-B., Jiang, L.-F., Li, G., Du, Z.-L., 2015. The phase transformation of $CuInS_2$ from chalcopyrite to wurtzite. Nanoscale Res. Lett. 10, 1–7.
Yang, C., Cho, K., 2021. Rapid and selective removal of Cs^+ from water by layered potassium antimony thiostannate. J. Hazard Mater. 403, 124105.
Yang, Y., Zheng, Z., Ji, W., Xu, J., Zhang, X., 2020. Insights to perfluorooctanoic acid adsorption micro-mechanism over Fe-based metal organic frameworks: combining computational calculation with response surface methodology. J. Hazard Mater. 395, 122686.
Zhang, H., Hodges, C.S., Mishra, P.K., Yoon, J.Y., Hunter, T.N., Lee, J.W., Harbottle, D., 2020. Bio-inspired preparation of clay–hexacyanoferrate composite Hydrogels as super adsorbents for Cs^+. ACS Appl. Mater. Interfaces 12, 33173–33185.
Zhang, H., Kim, Y.K., Hunter, T.N., Brown, A.P., Lee, J.W., Harbottle, D., 2017. Organically modified clay with potassium copper hexacyanoferrate for enhanced Cs^+ adsorption capacity and selective recovery by flotation. J. Mater. Chem. 5, 15130–15143.
Zhao, J., Islam, S.M., Hao, S., Tan, G., Stoumpos, C.C., Wolverton, C., Chen, H., Luo, Z., Li, R., Kanatzidis, M.G., 2017. Homologous series of 2D chalcogenides Cs–Ag–Bi–Q (Q= S, Se) with ion-exchange properties. J. Am. Chem. Soc. 139, 12601–12609.
Zhiznin, S., Timokhov, V., Gusev, A., 2020. Economic aspects of nuclear and hydrogen energy in the world and Russia. Int. J. Hydrogen Energy 45, 31353–31366.
Zhou, L., Xu, M., Yin, J., Shui, R., Yang, S., Hua, D., 2021. Dual ion-imprinted mesoporous silica for selective adsorption of U (VI) and Cs (I) through multiple interactions. ACS Appl. Mater. Interfaces 13, 6322–6330.